



Leppänen, J., Johansson, M. and Grassl, P. (2020) On the dynamic response of reinforced concrete beams subjected to drop weight impact. *Finite Elements in Analysis and Design*, 180, 103438. (doi: [10.1016/j.finel.2020.103438](https://doi.org/10.1016/j.finel.2020.103438))

There may be differences between this version and the published version. You are advised to consult the publisher's version if you wish to cite from it.

<http://eprints.gla.ac.uk/222570/>

Deposited on 25 August 2020

Enlighten – Research publications by members of the University of Glasgow
<http://eprints.gla.ac.uk>

On the dynamic response of reinforced concrete beams subjected to drop weight impact

Joosef Leppänen^{a,*}, Morgan Johansson^{a,b}, Peter Grassl^c

^a Department of Architecture and Civil Engineering, Chalmers University of Technology, SE-412 96 Göteborg, Sweden

^b Norconsult AB, Göteborg, Sweden

^c James Watt School of Engineering, University of Glasgow, Glasgow G128LT, UK

* Corresponding author. E-mail: joosef.leppanen@chalmers.se

Abstract

To improve the impact resistance of reinforced concrete structures, a detailed understanding of the dynamic response is required. This study investigates this impact resistance using experiments in combination with 3D non-linear finite element (FE) simulations. The experiments made use of high-speed photography and digital image correlation (DIC), while a damage-plasticity constitutive model for concrete was used in the FE simulations. Drop weight impact tests of simply supported reinforced beams made of plain concrete and fibre reinforced concrete were made, and it was shown that the addition of fibres reduced crack spacing, crack widths and mid-point deflections. For the FE approach, tetrahedral elements were shown to be well suited for capturing inclined shear cracks and the structural response obtained in experiments and analyses agreed very well. The FE analyses showed that the reinforcement strains were more localised for concrete with fibres, and hence predicted an increased risk of reinforcement rupture.

Keywords: concrete, fibres, drop weight impact, digital image correlation (DIC), CDPM2

23 **1. Introduction**

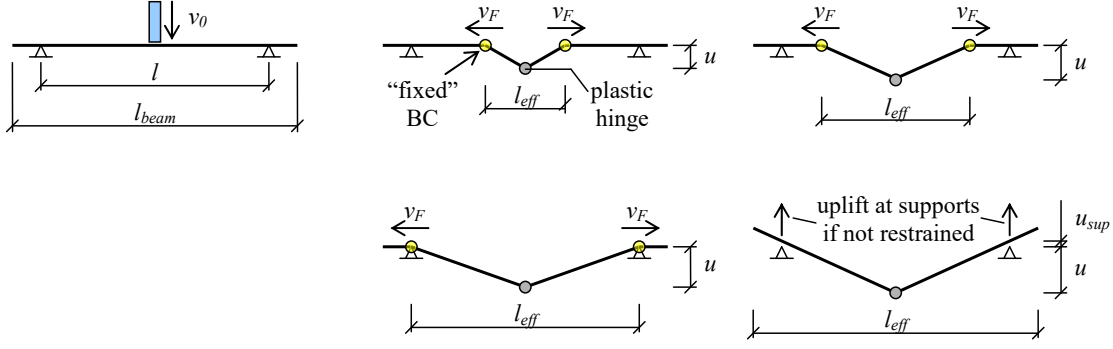
24 Understanding the response of reinforced concrete structures subjected to impulse loading (i.e.,
25 blast and impact) is essential for designing critical infrastructure with confidence. Concrete
26 cracking in tension, concrete crushing in compression, yielding of reinforcement, and interplay
27 between concrete and reinforcement interact in a very short period, often resulting in a complex
28 structural response. This response is difficult to predict without detailed experimental and
29 numerical analyses.

30 The structural response of an impulse loaded structure may be very different compared to when
31 subjected to a quasi-static load with the same geometric configuration. Due to the intense
32 energy released in a short time, different phenomena will occur that affect both the material and
33 structural response of the loaded structure. High strain rates cause the material in the structure
34 to become stiffer, stronger, and more brittle [1–3], while wave propagation effects at the same
35 time may greatly influence the structural response. Several studies [4–7] have noted that the
36 load capacity increases with increased load rate. The load capacity increase is partly due to
37 increased material strength as well as inertia effects causing a change in the structural response.

38 When a structure is subjected to a load, it takes time for this information to transfer within the
39 structure. This time lapse is the case in all structures and for all types of loading. However, the
40 information travels very fast within the structure (the shear wave velocity in concrete is
41 approximately 2300 m/s); consequently, it is only when rapid loading is applied that such so
42 called wave propagation effects will be important. In impact loading the impact force may be
43 very high but with a short duration – in the order of just a few milliseconds or less. This means
44 that all, or a large part, of the load may have been transferred to the structure before information
45 of the load application has reached all parts of the structure. For example, in an impact loaded
46 beam, there will be a notable lag in the time between impact and when the supports experience
47 the applied load. This lag also means that the initial deformed shape of the beam will be very

48 different compared to the same beam subjected to a static point load. Since it takes some time
49 for the information of the applied load to reach all parts of the structure and it takes time for the
50 structure to react, parts of the beam will initially be ‘unaware’ of both the support conditions
51 and the applied load.

52 This initial response is denoted as the local response [8] and the deformed shape will vary as
53 schematically illustrated in Fig. 1 [9]. Here, a plastic hinge is assumed to form in the section of
54 impact and the affected part of the beam responds as if it was a fixed beam with an effective
55 span length l_{eff} . Consequently, tensile stresses that may cause cracks will form at the top of the
56 beam. The effective span length increases with time and, therefore the stiffness and load
57 capacity of the beam will vary during the local response. The time it takes for the initial response
58 to develop depends on the beam length and average force propagation velocity v_F . This velocity
59 is considerably smaller than the shear wave velocity and decreases approximately
60 proportionally with increased beam slenderness (approximately 250 to 1000 m/s for
61 length/depth of the beam varying between 10 and 4) [10,11]. Eventually, the effective length
62 reaches the supports. If the beam is not vertically restrained, it will briefly lift up due to the
63 inertia forces gathered within the effective length [12]. Once the whole beam is affected (i.e.,
64 $l_{eff} = l_{beam}$), the overall response [8] is initiated in which a deformed shape approximately
65 corresponding to that of static loading is obtained. However, this takes some time and until then
66 the beam’s boundary conditions can be regarded as time-dependent fixed supports, where the
67 locations of these supports gradually move toward the free ends of the beam.



68

69 **Fig. 1.** Schematic illustration of how the deformed shape of an impact loaded beam
70 develops during the local response. Based on [9] and [12].

71 The capacity of a structure to withstand the effect of impulse loading mainly depends on its
72 ability to absorb the external energy applied by the load. Using a single degree of freedom
73 model and assuming plastic impact, the external energy acting on the beam can be
74 approximately determined as $W_e = m_w / (m_w + m_b) \cdot E_{k,0}$, where m_w is the mass of the drop weight,
75 m_b is the effective mass of the beam, $E_{k,0} = m_w \cdot v_0^2 / 2$ is the kinetic energy of the drop weight at
76 impact, and v_0 is the impact velocity [13]. Hence, the external energy applied to the beam will
77 decrease with an increased beam mass. To withstand the effect of impact, the external energy
78 should be balanced by the internal energy – $W_i = \int R(u) du$ – provided by the beam, where $R(u)$
79 is the load capacity as a function of the deflection u . Consequently, in an impulse-loaded
80 structure, the internal energy W_i (not the maximum load capacity) is essential to withstand the
81 load. In such structures it is usually preferred that the energy consumption of the structure is
82 provided by large deformations rather than large internal forces [14–17]. This arrangement is
83 ensured by designing the structure with regard to bending and providing it with a large plastic
84 deformation capacity. To fulfil the latter criterion, the structure should be designed so it does
85 not experience premature brittle failure, for example, due to shear. Hence, avoiding shear failure
86 in an impulse-loaded structure is essential and has been the focus of several studies [18–20]. A
87 potential problem here is that the mechanics of shear failure in impulse loaded structures are

88 not as well understood as failure due to bending [18] and several studies have noted that a
89 statically-loaded structure that fails due to bending may instead fail in shear when subjected to
90 impulse loading [18–20].

91 In the equation for the external energy, the mass of the impacting body is important. However,
92 the impacting body's geometric properties are also important and as such have been the subject
93 of several studies [21–25]. These studies have concluded that an increased radius on the drop
94 weight head results in increased contact stiffness, that this stiffness significantly influences the
95 impact force (force increase with increased stiffness), and that a decreased head radius leads to
96 more severe local concrete damage at the impact zone. However, the contact stiffness has only
97 minor effect on the resulting impulse, impact energy, and resulting mid-span displacement of
98 the loaded structure. Furthermore, a flat head is sensitive to the inclination angle of the drop
99 weight [24], suggesting that it is preferable to use a head with a radius that is not too large.

100 If the beam's internal energy capacity is high enough (i.e., $W_i \geq W_e$), the structure can withstand
101 the effect of impulse loading and reach its maximum deformation when $W_i = W_e$. However, due
102 to elastic energy gathered in the structure, it will rebound in the opposite direction of the load,
103 and the beam will lose contact with its supports if it is not restrained. Consequently, restrained
104 boundary conditions may greatly affect the response of the rebounded beam, although it will
105 have negligible effect on the response up to maximum deformation in the direction of the
106 applied load.

107 Simplified calculation tools, based on spring-mass models of one or several degrees of freedom,
108 are commonly used in practical design of impulse-loaded structures [15–17,26]. Such tools are
109 advantageous in the sense that they provide an improved understanding to the fundamental
110 physics behind complex events such as impact-loaded structures. Furthermore, they are fast and
111 therefore may be very powerful since, once defined, it is easy to make many calculations

quickly. The improvement of such simplified methods is also the subject of several studies [8,9,23]. However, to understand in detail what happens during impact loading, more detailed models – e.g., FE models using 3D continuum elements – may be needed that correctly describe more complex phenomena such as concrete cracking and crushing, reinforcement yielding, and loss of bond. Although such tools are potentially powerful, experiments are still needed to check whether the FE results correspond to experimental results. Therefore, FE analyses should be regarded as a complement to experiments; that is, even if both methods have their advantages when used alone, they are even more powerful when used together. In the present study, reinforced beams of plain and fibre reinforced concrete subjected to impact loading were tested. The test set-up was designed for the specimens to obtain a bending mode response and to avoid shear failure with the purpose to use these results as a benchmark for nonlinear FE analyses.

Drop weight impact tests have been widely used to experimentally investigate the response of concrete beams [8,18,19,27–34] recorded in the form of global quantities such as impact force, support reaction force, midspan deflections, and final crack patterns. Recently, digital image correlation techniques (DIC) [35] have been used to investigate the evolution of crack patterns in impact tests of concrete beams reinforced with traditional steel bars (RC) [10,36]. This technique makes it possible to reproduce the strain field on the concrete surface and therefore provide improved understanding of the dynamic response of the loaded structure. Here, DIC was used to monitor the crack evolution of RC and steel fibre reinforced concrete beams reinforced with traditional steel bars (FRC). This experimental study provides in depth information about the response of concrete subjected to impact loading and a benchmark for evaluating the performance of numerical modelling.

Numerical modelling approaches for evaluating the detailed nonlinear response of concrete structures subjected to impact loading are commonly based on the finite element method, which is used to model concrete and steel reinforcement as interacting phases. For concrete, models

for cracking and crushing are commonly based on plasticity [37,38], damage mechanics [39,40], or combinations of these two [41–45]. Alternative approaches include micro-plane based models [46,47] and discrete methods [48,49].

FE analyses use an implicit or explicit solution method [50]. In the implicit method, equilibrium is based on information in both the current and previous increments, so that an iteration procedure is needed to find the equilibrium. In the explicit method, the equilibrium in the current increment is based solely on information in previous load increments, and therefore, an iteration procedure is not required. Hence, using an explicit method may be an effective way to avoid numerical convergence problems encountered when using an implicit method to solve nonlinear problems. However, with the explicit method very small time steps have to be used to obtain a stable solution. When modelling impact loading, small time steps are anyway needed to correctly capture the response. Consequently, an explicit solution method is suitable to model impact loading.

Here, in the numerical analyses, the damage-plasticity model CDPM2 proposed by the third author [51,52], and implemented in LS-DYNA as *MAT_CDPM (*MAT_273), was used as the concrete constitutive model. This model reproduces many of the key characteristics of concrete – e.g., softening in tension and low confined compression with reduction of stiffness and permanent strains, and pressure sensitive strength and deformation capacity for triaxial compression [51]. This model also reproduces the strain rate dependence of concrete, which is important for modeling the dynamic response of structures [52].

In LS-DYNA, several different types of damping are available; e.g. Rayleigh damping and artificial bulk viscosity. The former method is a mass and stiffness proportional viscous damping that presents a common approach to simulate the energy dissipation in structural dynamics, while the latter is a method used to handle discontinuous shock waves in materials.

In an impulse loaded structure, it is usually the initial response that is of interest; i.e. the peak

deformation. Hence, the effect of mass weighted damping is small and can often be neglected [14]. However, for structures subjected to very high strain rates ($>10 \text{ s}^{-1}$), e.g. high-speed projectiles impact on concrete slabs, it has in [53] been shown that the bulk viscosity can have a significant influence on the resulting projectile penetration depth. There, it is also argued that bulk viscosity, due to both physical aspects and numerical reasons, must be included in the analysis. This statement, though, is contradicted by [54], where it is instead argued that bulk viscosity should not be included but an enhanced constitutive model should be used. For impulse loading of RC and FRC structures, it is common to use hexahedral elements in the numerical model in the FE program LS-DYNA [24,55–58]. However, it is well known that the element type affects the crack patterns [59,60]. It was shown that the use of tetrahedral elements made it easier to follow diagonal shear cracks. In addition, CDPM2 has been shown to perform well for quasi-static loading with tetrahedral elements [61]. Studies using tetrahedral elements for dynamically loaded concrete structures have been carried out in LS-DYNA and other FE programs [62–64]. Response of steel fibre reinforced concrete to impact and blast loading can be predicted accurately using tetrahedral elements in three-dimensional numerical studies [62]. A model based on continuum mechanics, rate dependent microplane, and standard tetrahedral finite elements has accurately predicted the complex dynamic fracture process of concrete [63]. Similarly, using tetrahedral elements can predict tension-shear damage and mixed-mode fracture in solids subjected to dynamic loading [64]. Merging the material model CDPM2 with tetrahedral elements has satisfactorily reproduced impact loading with respect to the bond between steel bars and concrete, merged and coincident with slip [13]. Compared to hexahedral elements, tetrahedral elements in LS-DYNA with CDPM2 seem to capture better diagonal shear cracks due to impact loading [65]. However, these studies neglect the strain rate effects both for the concrete and the steel bars [13,65].

This paper investigates the difference in results when using hexahedral and tetrahedral elements for RC and FRC structures subjected to impact loading when using the previously developed material model CDPM2, including strain rate effects (for concrete and steel rebar). Drop weight (made of steel) impact tests were carried out on plain concrete and fibre reinforced concrete beams with ribbed steel bars. A combination of high-speed photography and DIC made it possible to compare these drop weight test results of crack patterns and structural response with FE analyses. The aim of this comparison was to find whether CDPM2 can sufficiently model impact loaded RC and FRC structures and to use CDPM2 to study phenomena that are difficult to extract from experiments only, such as reinforcement strains. Specifically, CDPM2 was used to study the effect of strain localisation and development of plastic hinge in an impact-loaded structure made of fibre-reinforced concrete and plain concrete.

2. Experimental test set-up

In the present study, a 10.1 kg drop weight, released from a height of 5.5 m, impacted simply supported beams placed on rollers (Fig. 2). The test specimens were small: the length of the beams was 1.18 m, the length of the span was 1.0 m, and the beam cross section was 0.1 x 0.1 m. The beam height corresponds to a height of a slab in, e.g., a Swedish civil defence shelter with a scale factor of 1:3.5. The beams were reinforced with 2+2 ribbed steel bars with a nominal diameter of 6 mm resulting in a reinforcement ratio of about 0.7 %. The roller supports had a diameter of 70 mm and were free to roll against their supports, which were made of thick steel plates. The beams were not restrained, so during the test the beam could obtain a rigid body movement upwards once rebounding occurred – i.e., the beam's boundary conditions were not the same for downward and upward deformation. The main reason for this test set-up was to avoid restraint moments. This was deemed to be an acceptable solution since the purpose here was to study the beam's structural response when deforming in the direction of the applied load (i.e., downward). This configuration also made it easy to correctly position the beams in

the test set-up, providing for an effective testing procedure with good repeatability. No impact or reaction forces were measured.

A beam is normally restrained at the connections, and in impact tests typically an upper restraint is added to the supports to prevent rebounding [8,18,19,28,31]. However, in impact tests simplify support conditions are also often used, by using only simply supported beams without an upper restraint [30,32–34], and some studies have used both upper restrained and unrestrained beams [27,29]. Simply supported boundary conditions cannot capture the rebound effect. Typically, the initial deflection causes the most damage and therefore is the most dangerous. Furthermore, small scale experiments are commonly used for impact tests – small cross sections, e.g., 0.1 m x 0.1 m [27,32,33] or 0.15 x 0.15 m [29,34] and span lengths up to 1.0 m.

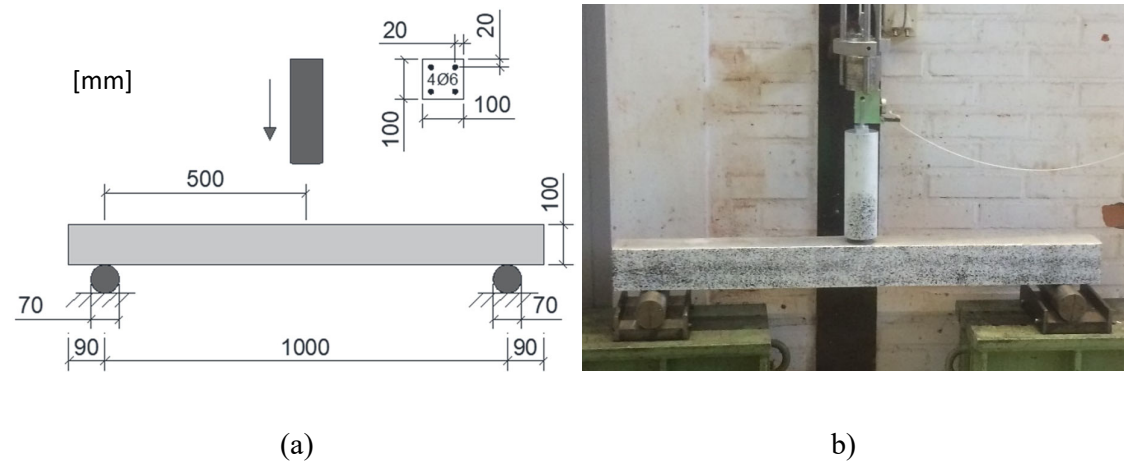


Fig. 2. Experimental test set-up: (a) geometry, and (b) photo of beam and drop weight with speckled pattern applied.

The experiments analysed in this paper were part of a larger experimental series [12,36]. From this series of experiments, five RC and four FRC beams were selected for the present investigation.

229 A high-speed camera was used during the drop weight impact tests. Images were taken every
230 0.2 ms (i.e., 5000 frames per second, fps). This frame rate is not high enough to capture what
231 happens locally in the impact zone, but it is accurate enough to obtain information about the
232 global response of the beam and its crack propagation. Only half of the beam was recorded to
233 obtain good resolution. DIC with the software GOM Correlate ARAMIS [66] was used to
234 analyse the high-speed camera images. This technique is commonly used to measure
235 deformations and strain fields of a surface. The basic idea is to analyse the change of a surface
236 speckle pattern in a series of digital images taken during the test. This analysis is done by
237 tracking the position of discrete pixel subsets of the speckle pattern. If the time between each
238 image taken during the test is known, the deformations, strains, velocities, and accelerations
239 can be measured. To create the surface component in GOM Correlate, a facet size of 15 pixels
240 and a point distance of 10 pixels were used for the RC beam. For the FRC beam, a facet size of
241 15 pixels and a point distance of 5 pixels were used. Each pixel had a point distance of
242 approximately 0.6 mm in GOM Correlate. DIC was used for all beams tested to determine crack
243 patterns, deformed shape and midpoint-deflection. In addition, DIC was used to determine that
244 the average impact velocity of the drop weight was 10.35 m/s.

245 The specimens were cast with self-compacting concrete (Table A.1). The fibre reinforced
246 concrete, 40 kg/m³ ($V_f = 0.5\%$) of Dramix steel fibres, was 35 mm long and 0.55 mm in
247 diameter. The compressive strength f_c and tensile strength f_t and fracture energy G_F were tested
248 according to standard procedures [67–70].

249 For the plain concrete, wedge splitting tests [69] were used to determine the fracture energy.
250 For the fibre reinforced concrete, RILEM beams were tested according to [70], and the force
251 and crack mouth opening displacement (CMOD) were recorded (Fig. A.1).

Material testing on the day of the impact experiments (45 days after casting) gave the following mean values for the three test specimens for each test: $f_c = 45.5$ (49.7) MPa, $f_t = 3.28$ (3.55) MPa; and $G_F = 113$ (1676) Nm/m². The values given refer to RC (FRC).

Material tests for the reinforcement were also conducted. The reinforcement was coil reinforcement of class C [71] with a characteristic yield strength of 500 MPa. The stress-strain curve for the tested reinforcement bars are shown in Fig. A.2. The data for the drop weight used in the experiments are shown in Table A.2.

3. FE analyses

3.1 Concrete constitutive model

The previously developed concrete damage-plasticity model 2 (CDPM2) [42,51,52] was used. This constitutive model can reproduce many features of the failure process of concrete, which are important for modelling structures subjected to impact loading. The model has been shown to accurately reproduce the effect of confinement on strength and strain capacity in compression, which is important for capturing the effect of lateral confinement generated below the impact point. The model can describe the stiffness change for a transition from tension to compression and vice-versa, which occurs often in dynamic simulations due to the effect of wave propagation and reflection. In addition, the model describes the dependence of tensile and compressive strength on strain rate [52].

The techniques in CDPM2, which can capture these features, are outlined briefly. In CDPM2, the stress evaluation is based on a combination of damage mechanics and elasto-plasticity. With respect to plasticity, the effective stress in the undamaged material is determined. The damage is then used to evaluate the nominal stress by applying tensile and compressive damage variables to positive and negative parts of the principal effective stress, respectively.

The plasticity part of the model is formulated in the effective stress space by means of the Haigh-Westergaard stress coordinates, which are the volumetric effective stress $\bar{\sigma}_v$, the length

of the deviatoric effective stress $\bar{\rho}$ and the Lode angle $\bar{\theta}$ [72]. The yield surface is based on an extension of the static strength envelope [73], which was shown to reproduce experimental results well. This strength envelope is characterised by curved meridians and deviatoric sections varying from almost triangular in tension to almost circular in highly confined compression (Fig. 3).

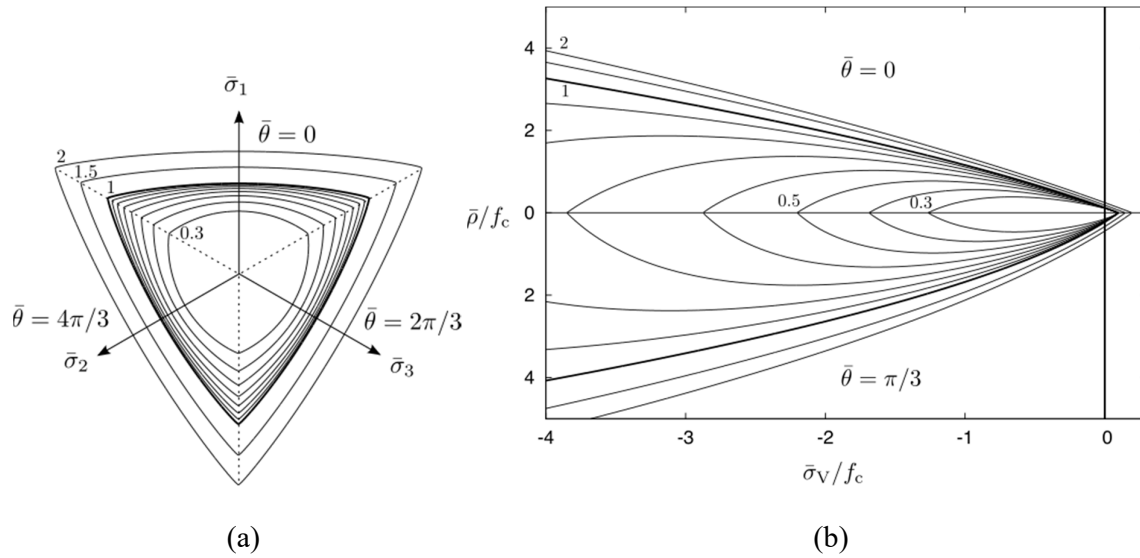


Fig. 3. Evolution of the yield surface for varying values of the hardening variable q_h (from 0.3 to 2), which is smaller than 1 in the pre-peak and larger than 1 in the post-peak regime: (a) deviatoric section for a constant volumetric stress of $\bar{\sigma}_v = -f_c/3$ and (b) meridians at $\bar{\theta} = \pi/3$ (compression) and $\bar{\theta} = 0$ (tension). A thicker line indicates static strength surface where $q_h = 1$.

Based on this static strength envelope, static pre- and post-peak regimes were defined. In the pre-peak regime, the yield surface is capped both in hydrostatic tension and compression. At peak, the static strength envelope previously proposed in [73] is reached, which is open in hydrostatic compression. In the post-peak regime, the yield surface further extends with the shape being similar to the strength envelope. The hardening in the post-peak regime is controlled by the hardening modulus H_p . The greater the value of H_p , the smaller the contribution of plasticity in the post-peak regime.

In quasi-static simulations, damage is initiated once the strength envelope is reached. For dynamic simulations in which the strain rate dependence of concrete is considered, damage initiation is made dependent on the strain rate: the greater the strain rate, the greater the delay of the damage initiation [52]. This is achieved by dividing the rates of the equivalent strains by a strain rate dependent factor which is equal to one for quasi-static loading and increases with increasing strain rate. This way to model the rate dependence of strength is a simplified version of the often used damage delay approach [74–76]. A visco-elastic model to describe the rate dependence of the elastic response as used, for instance, in [75,77] was not considered in this study. Consequently, there is no damping in the analyses due to sudden changes in strain rate as they occur during cracking. Consequently, the strength at which damage (and softening) is initiated exceeds the static strength of the envelope (Fig. 4). This means that for dynamic loading, the pre and post-peak regimes differ from those defined by the static strength envelope. For this technique to produce reasonable results in the pre-peak in compression, H_p must be set to a large value so that the plastic strain before the onset of damage remains small. Therefore, $H_p = 0.5$ was used. The effect of strain rate on compressive and tensile strengths were modelled using equations proposed in Model Code 1990 [78] and [2]. All the equations used in CDPM2 for modelling the strain rate effect are shown in [52] in detail.

Once damage is initiated, the response is a combination of the theory of plasticity and damage mechanics. Evolution laws for tensile and compressive damage are formulated as functions of positive and negative parts of the principal effective stress so that tensile and compressive softening responses can be described independently. Mesh-independent results are obtained using the crack-band approach [79]. In this approach, the function for the tensile damage variable is derived from a bilinear stress-crack opening ($\sigma - w_c$) curve, so the results of analyses of tensile failure in which strains localise in mesh-dependent regions are independent of the finite element mesh [79–81]. Consequently, the finer the mesh, the larger the strain at constant

crack opening. If the strain rate in cracked elements were used, a strong mesh-dependence would be obtained, because, in the crack band approach, for a constant crack opening the strain is a function of the element size. Therefore, once damage is initiated in a material point, the strain rate effect on strength is set constant to the value reached in that time step.

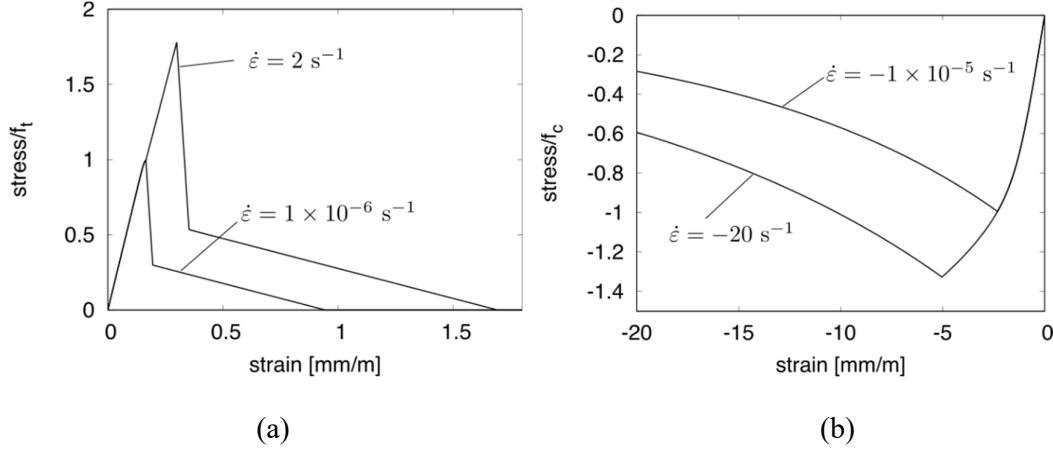


Fig. 4 Effect of strain rate on softening responses used to determine damage variables: (a) bilinear stress-crack opening curve used to determine tensile damage variable and (b) exponential stress-inelastic strain curve used to evaluate the compressive damage variable.

The tensile fracture energy of concrete G_F is defined as the area under the stress-crack opening curve for quasi-static loading (strain rate factor equal to one). For the present bilinear curve, this results in $G_F = (f_t w_{FI} + f_{tI} w_F)/2$. For the default in CDPM2, $f_{tI} = 0.3 f_t$ and $w_{FI} = 0.15 w_F$, so $G_F = 0.225 f_t w_F$. Thus, the crack opening threshold is related to the area under the stress-crack opening curve (fracture energy) as $w_F = 4.444 G_F/f_t$. Within the crack band approach in CDPM2, the crack opening w_c is converted into an inelastic strain $\epsilon_c = w_c/h_b$, where h_b is the assumed width of the band in which strains localise. For linear hexahedral elements with reduced integration used in this study, the band width is set to $h_b = \sqrt[3]{V_e}$, where V_e is the element volume. For linear tetrahedral elements, the band width is $h_b = 1.79 \sqrt[3]{V_e}$. This practical approach produces similar global energy dissipations for tetrahedral and hexahedral meshes [61], which was acceptable for the present comparison. More refined approaches in which the

band width is determined based on principal directions of stresses and/or strains have also been presented [82].

The compressive damage variable is linked to a stress-inelastic strain curve, since the deformation patterns in the compressive zones of applications dominated by bending are often mesh-size independent [51].

CDPM2 requires many input parameters, which can be divided into groups related to the elastic, plastic and damage parts of the model. In the present work, most of these parameters are set to their default values as described, where it was shown that these parameters provide a good match with experimental results for quasi-static loading [51]. Some of the parameters are directly linked to experimental results, such as the f_t and f_c (Section 2). Young's modulus was calculated according to EN 1992-1-1 [71] as $E_{cm} = 22 \cdot (f_{cm}/10)^{0.3}$, and the density ρ was set to 2400 kg/m³. The damage threshold w_f was adjusted to match material data available for the different groups of analyses. For plain concrete, w_f was calculated using the fracture energy stated in Section 2. For fibre reinforced concrete, three point bending tests were performed as described [70]. Then, inverse analysis was used to determine the input parameters for the bilinear stress-crack opening law in CDPM2 (Fig. A.1). In CDPM2, the default value of the inelastic strain threshold ε_{fc} results in a very brittle response in compression. To avoid numerical difficulties, it is sometimes required to choose a more ductile compressive response to avoid premature failure in regions close to supports or applied loads. Therefore, for tetrahedral meshes, this parameter was set to $\varepsilon_{fc} = 0.001$, whereas for hexahedral meshes the default $\varepsilon_{fc} = 0.0001$ was used.

3.2 Reinforcement constitutive model

The material model Johnson-Cook [83] was used to describe the stress-strain response of the reinforcement steel. The yield stress is expressed as follows:

$$\sigma = (A + B \cdot \varepsilon_p^n)(1 + C \cdot \ln \dot{\varepsilon}^*)(1 - T^{*m}),$$

366 with five material constants: A , B , n , C and m . Here, ε_p is the equivalent plastic strain, $\dot{\varepsilon}^* = \frac{\dot{\varepsilon}}{\dot{\varepsilon}_0}$
367 is the dimensionless plastic strain rate and T^* is the dimensionless temperature.

368 The constants A , B , and n (expression in the first set of brackets) give the stress as a function of
369 strain for $\dot{\varepsilon}^* = 1$ and $T^* = 0$, which correspond to the static material tests. The input material
370 parameters of the model ($A = 400$ MPa, $B = 450$ MPa and $n = 0.21$) were chosen by fitting
371 material tests of the reinforcement bars (Fig. A.2). The strain rate was modelled per previous
372 recommendations [84], with quasi-static threshold strain rate $\dot{\varepsilon}_0 = 10^{-4}$ and the strain rate
373 constant $C = 0.017$. Temperature effects were not considered in the FE analyses.

374 There was no need to model rupture of the reinforcement as the effective plastic strains were
375 expected to be smaller than the ultimate strain. The analyses used the following values:
376 $E = 200$ GPa, Poisson's ratio $\nu = 0.3$ and $\rho = 7850$ kg/m³.

377 3.3 Numerical model

378 Three-dimensional numerical analyses of the drop weight impact test were conducted using the
379 software LS-DYNA [85]. An explicit method based on central difference scheme [85] with an
380 automatic time step control was used in the numerical analyses. The time step was in the order
381 of $3.5 \cdot 10^{-4}$ ms and $2.3 \cdot 10^{-4}$ ms for hexahedral and tetrahedral elements, respectively. Default
382 values in LS-DYNA [85] were used for both Rayleigh damping (no damping) and artificial bulk
383 viscosity (1.5 for quadratic and 0.06 for linear viscosity coefficients). For the impact tests
384 studied, the maximum strain rate was in the order of about $1\text{-}10$ s⁻¹, and therefore bulk viscosity
385 was not expected to influence the results from the FE analyses. A sensitivity analysis was
386 performed, which confirmed this expectation.

387 The model consisted of four parts: the roller supports, the concrete beam, reinforcement
388 embedded in the concrete beam, and the drop weight (including the radius of the head), see
389 Fig. 5. For the beams and the supports, solid hexahedral and tetrahedral elements were used.

The hexahedral and tetrahedral elements were 8-node and 4 node solid elements, respectively, with one integration point. The drop weight was modelled with hexahedral mesh. The reinforcement was modelled with beam elements using Hughes-Liu formulation [85] with circular cross section. Hourglass control was needed to ensure stability of hexahedral elements, and the Belytschko-Bindeman formulation [85] was used with default input parameters. Convergence of the element size was previously studied for the hexahedral and tetrahedral meshes, with element edge lengths of one side of 2.5 mm (only for hexahedral), 5 mm, 10 mm, and 20 mm [65]. In this study, the same geometries of the beam and drop weight were used; the drop heights, though were different (2.5 m and 5.0 m). It was concluded that an element edge length of 5 mm for both hexahedral and tetrahedral mesh were adequate to accurately represent the deflections and crack patterns. Thus, in this study an element length of 5 mm for both element types was chosen, which resulted in about 100000 elements and 900000 elements for the beam with hexahedral elements and tetrahedral elements, respectively.

To simulate the simply supported boundary conditions, rollers were fixed at the bottom and an automatic surface to surface contact, based on Taylor and Flanagan [85], without friction was used between the drop weight and the concrete beam. The same contact definition was used between the beam and the rollers.

The reinforcement was modelled with 5 mm beam elements assuming perfect bond between reinforcement and concrete, which has been shown to provide acceptable results [13]. The same nodes were used for concrete and reinforcement elements for both FE models.

The drop weight and the roller supports were modelled to be elastic: $E = 200$ GPa and $\nu = 0.3$. A small hole was drilled in the drop weight where an accelerometer (not used in the tests) was attached. This hole was not included in the FE model. Hence, to account for this, the steel

density of the drop weight was adjusted so that the mass corresponded to the mass in the experiments ($\rho = 7753 \text{ kg/m}^3$).

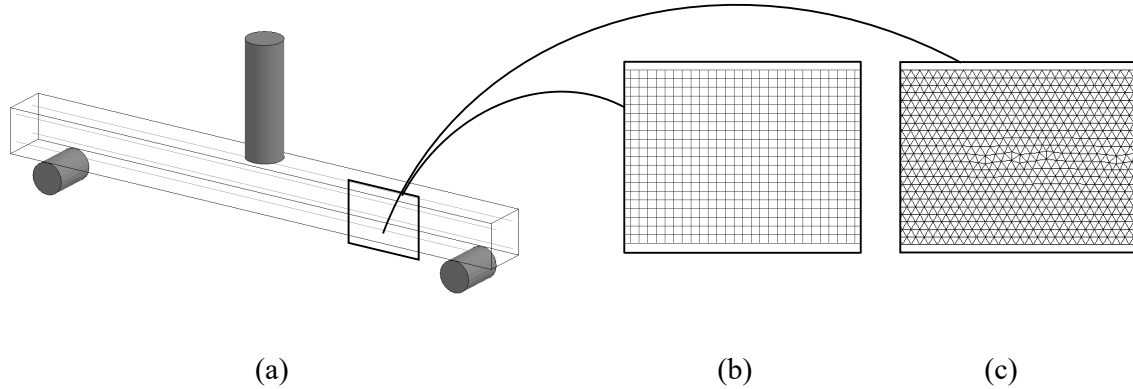


Fig. 5. Numerical model used in the FE analyses: (a) 3D model, (b) hexahedral mesh, and (c) tetrahedral mesh.

4. Results

The midpoint deflections obtained from DIC and FE analyses for RC and FRC beams are compared with experimental results (5 RC and 4 FRC) in Fig. 6; dashed lines in the figure indicate the beams used to compare crack patterns in Fig. 7 and Fig. 8 and the initial relative deformation in Fig. 9. This comparison shows that in general the beam deflections can be modelled effectively using CDPM2. However, the maximum midpoint deflection is overestimated using hexahedral elements. For the drop weight tests with RC beams, the maximum midpoint deflections were between 21 and 25 mm, with an average value of about 23 mm and in the FE analysis the maximum midpoint deflection was 29 mm using hexahedral elements. However, when using tetrahedral elements, the maximum midpoint deflection was 25 mm, which is very close to the experimental results.

For the FRC beams, it was found that the addition of fibres decreased the maximum midpoint deflection; and in the tests the maximum midpoint deflections were between 18 and 20 mm,

with an average value of 19 mm. In the FE analysis, the maximum midpoint deflection was 25 mm and 22 mm using hexahedral and tetrahedral elements, respectively.

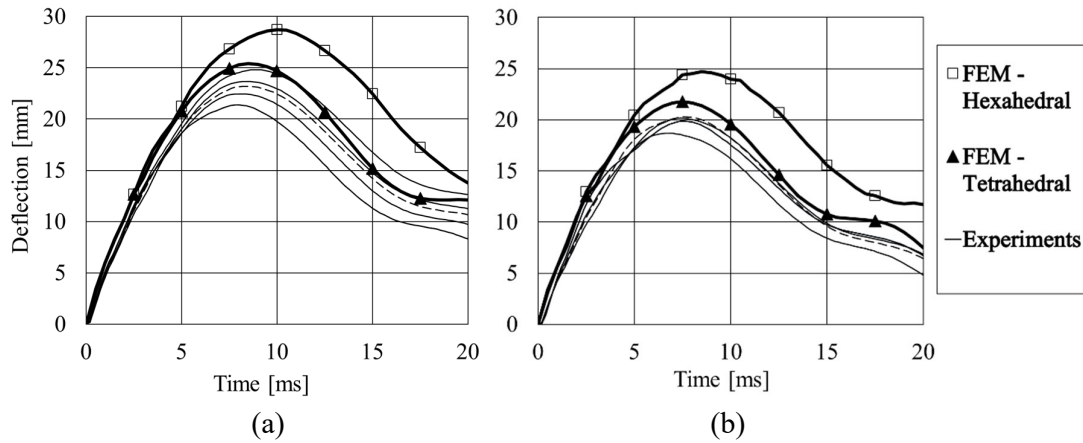
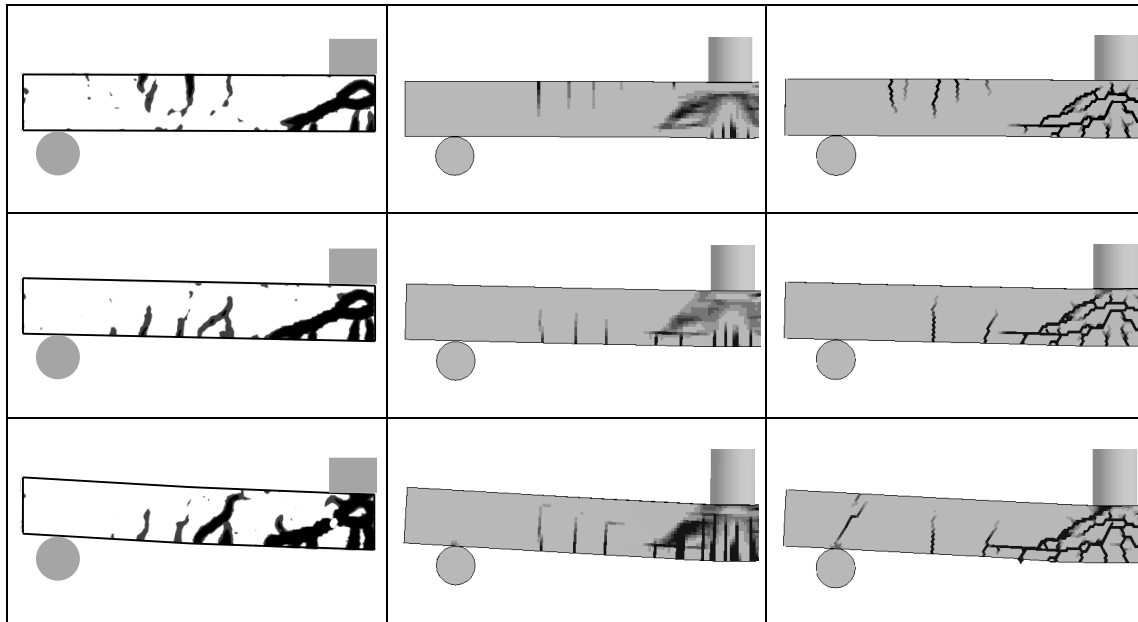


Fig. 6. Deflection in the midpoint of the beams, comparison with experiments (5 + 4 beams) and FE analyses using hexahedral and tetrahedral elements, (a) RC beams, and (b) FRC beams. Dashed lines correspond to the experimental beams used to compare crack patterns in Fig. 7 and Fig. 8 and initial relative deformation in Fig. 9.

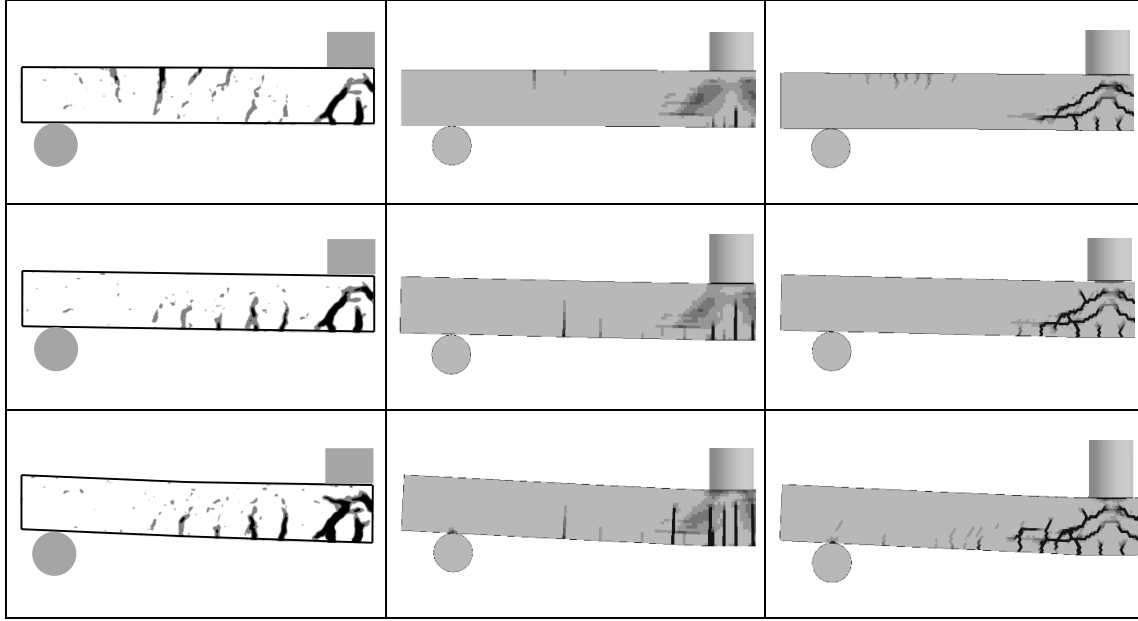
DIC made it possible to study the crack propagation as a function of time in the experiments. Here, just two beams from the experiments, one for RC and one for FRC, are presented. In Fig. 7, DIC and FE show the crack patterns at an initial stage and the stage at maximum deflection. In the DIC analyses, black indicates a crack visible to the eye (approximately 0.1 mm). In the numerical analyses the maximum principal strains were plotted and black corresponds to the cracking strain: $\epsilon_{\text{crack}} = 0.017$ (for tetrahedral elements).



(a) (b) (c)

Fig. 7. Comparison of DIC (dashed line in Fig. 6a) and FE-analyses for RC beam. (a) DIC, (b) hexahedral elements, and (c) tetrahedral elements. Time from impact: first row after 0.6 ms; second row after 2 ms; and third row after 9 ms.

Similar analyses were carried out for the FRC beams (Fig. 8). The response was very similar to the responses of the RC beams. However, the crack widths obtained using FRC are smaller than in the RC beam, both in the experiments and in the FE analysis. In the FE analysis, the early stage cracking is accurately captured (same concept as for RC shown in Fig. 7).



(a) (b) (c)

Fig. 8. Comparison of DIC (dashed line in Fig. 6b) and FE-analyses for FRC beam. (a) DIC, (b) hexahedral elements, and (c) tetrahedral elements. Time from impact: first row after 0.6 ms; second row after 2.0 ms; and third row after 8.0 ms.

The numerical analyses of the hexahedral elements show that the crack tend to follow the mesh and that the diagonal shear cracks cannot be captured as well as with tetrahedral elements.

Initially, bending cracks form at the bottom of the beam and shear cracks form close to the impact point. Then, bending cracks form at the top of the beam at a distance of roughly one-fourth of the span length from the support. The appearance of bending cracks at the top of the beam is due to wave propagation effects as schematically shown in Fig. 1. In Fig. 9, the relative deformation, $u_{rel}(x,t) = u_{mod}(x,t)/u_{max}$, from DIC and FE analyses using hexahedral elements in the RC beam is compared for the first 2 ms of loading. In the initial stage, the beam lifts at the supports. This effect, however, has been negated in Fig. 9 by setting $u_{mod}(x,t) = u(x,t) - u_{support}(t)$. The relative deformation along the beam shows that the beam has very high positive curvature beneath the drop weight and a negative curvature at the top soon

after impact. After the first two milliseconds, the deformed shape of the beam approaches that of a simply supported beam subjected to a static point load, with a plastic hinge in the middle of the beam. The relative deformation can be captured very effectively both in the DIC and the FE analyses and corresponds well with that shown in Fig. 1.

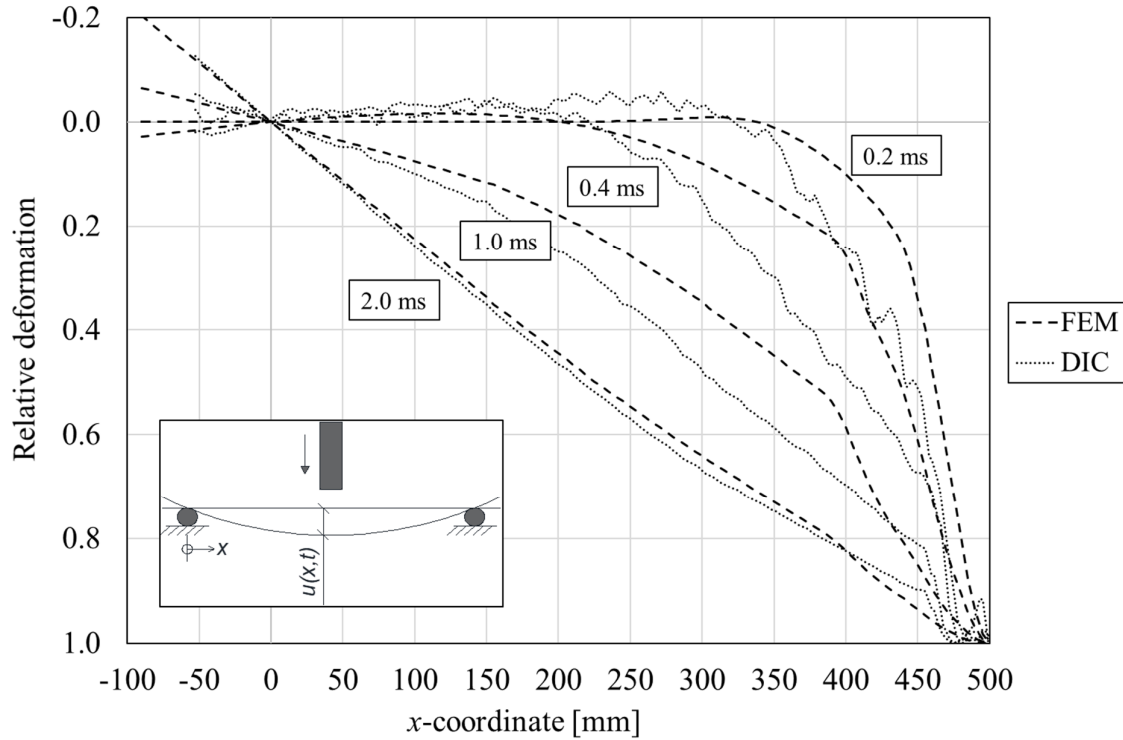
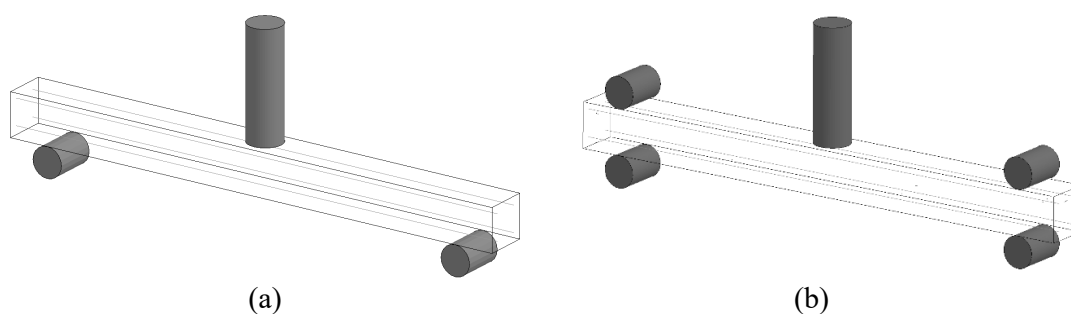


Fig. 9. Relative deformation for RC. Comparison with DIC (dashed line in Fig. 6a) and FE analyses (hexahedral elements) for the first 2 ms after impact.

Based on the observations made above, it can be concluded that the FE model using tetrahedral elements effectively reproduces the results obtained in the experiments both for RC and FRC beams. Accordingly, it is also possible to use the FE analyses to further complement the experiments; that is, they can be used to study different settings or phenomena that otherwise may be difficult to study using experiments alone. The influence of different boundary conditions, the impact force, the support reactions, and the strain localisation in the reinforcement were studied using only FE analysis.

484 The effect of different boundary conditions was studied with FEM for the RC beam using
 485 tetrahedral elements. The beams were supported on rollers – one beam was unrestrained and
 486 the other beam had an upper restraint to prevent upward movements at the support (Fig. 10).



487 **Fig. 10.** Numerical models used in FE analyses for study boundary conditions (a)
 488 unrestrained beam (same model as in Fig. 5), and (b) restrained beam.

489 The deflections from the FE analyses at the support and the midpoint deflection for the
 490 boundary conditions with and without upper restrain are compared in Fig. 11. In Fig. 11 (a), the
 491 beam deflections, in the initial contact point between bottom roller and the beam, at the bottom
 492 support are compared; in Fig. 11 (b), the midpoint deflections at the top of the beam for the two
 493 models are compared. The results show that the behaviour of the beam is hardly affected by the
 494 upper restraint for the first 15 ms, which is the time when the beams start to lift from their
 495 supports and the midpoint deflections start to deviate, after approximately 17 ms. These results
 496 show that the effect of the upper restrain has negligible effect on the midpoint deflection before
 497 rebounding occurs even if the unrestrained beam initially lifted from the supports for a few
 498 milliseconds. In addition, the restrained beam seems to have a small deflection at the support,
 499 but this deflection is due to the rotation of the beam at the support – i.e., the beam is in contact
 500 with the support at all times.

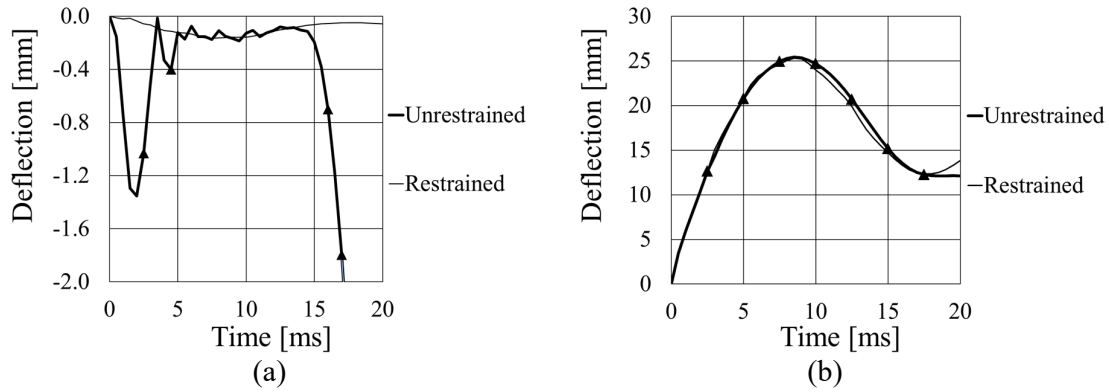


Fig. 11. Comparison of deflections with FE analyses with different boundary conditions
(a) at the support, and (b) midpoint deflections. Positive direction is downwards.

The effect on crack propagation due to different boundary conditions is compared in Fig. 12. As the crack propagation is very similar and independent of boundary conditions, the upper restraint had very little effect on the crack propagation for the first 15 ms – i.e., the time when the unrestrained beam started to lift from its supports. The boundary condition may affect the response of the rebounded beam. However, the boundary condition has negligible effect on the response up to the maximum midpoint deflection in the direction of the applied load, which often causes the most damage for the beam.

for RC and FRC beams and can be compared to the momentum of the dead-weight just prior to impact: $p_0 = m \cdot v = 10.1 \cdot 10.35 = 105 \text{ Ns}$.

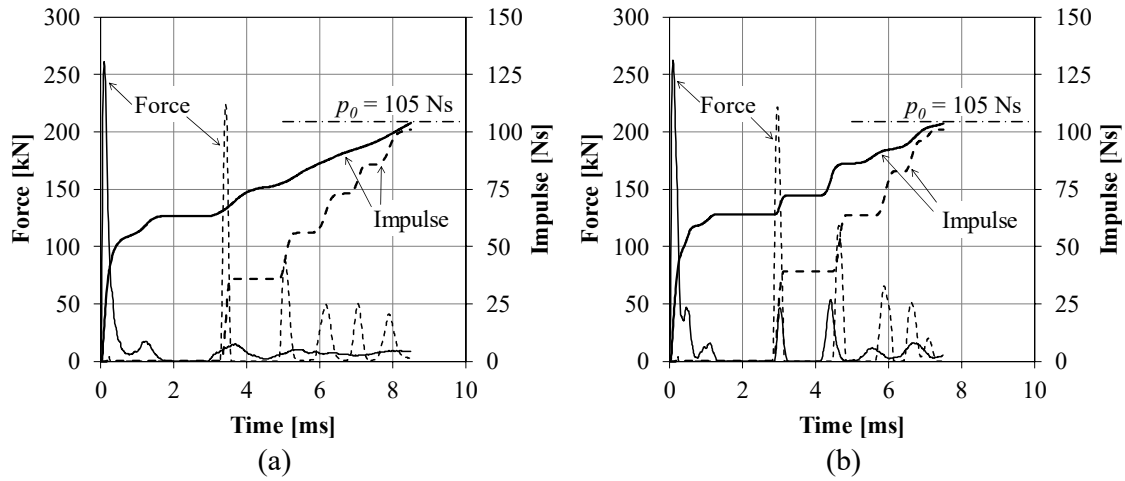
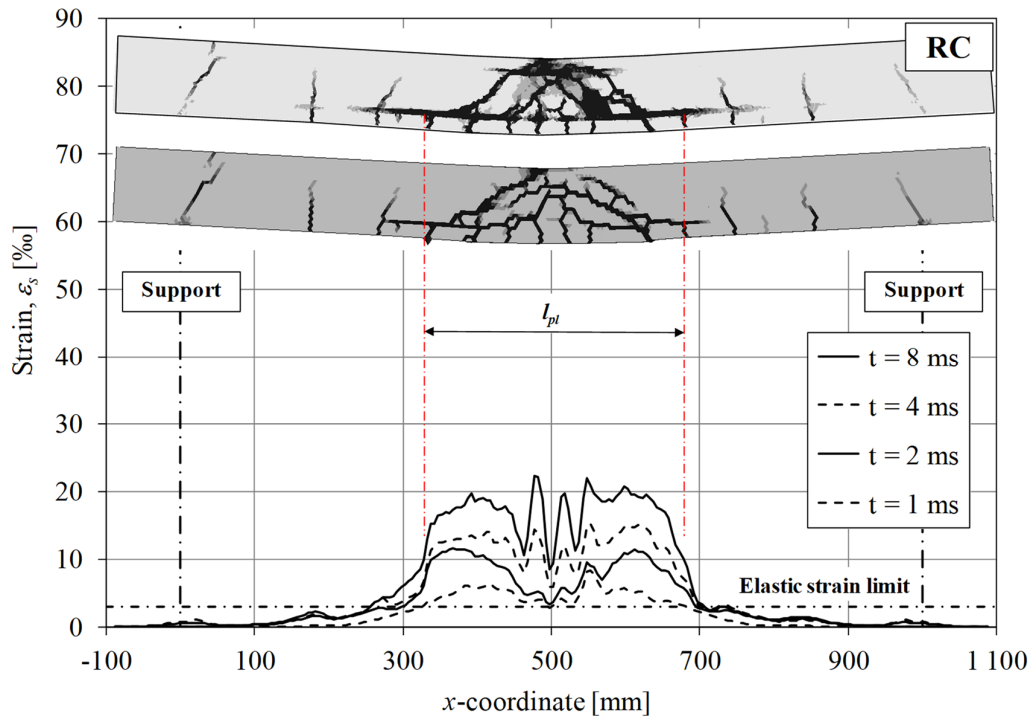


Fig. 13. Force and impulse from impact force (solid lines) and total support reaction (dashed lines) from FE analyses using tetrahedral elements of (a) RC beam and (b) FRC beam. The momentum p_0 of the drop weight just prior to impact is marked as comparison. Impact or support reaction forces were not measured in the experiments.

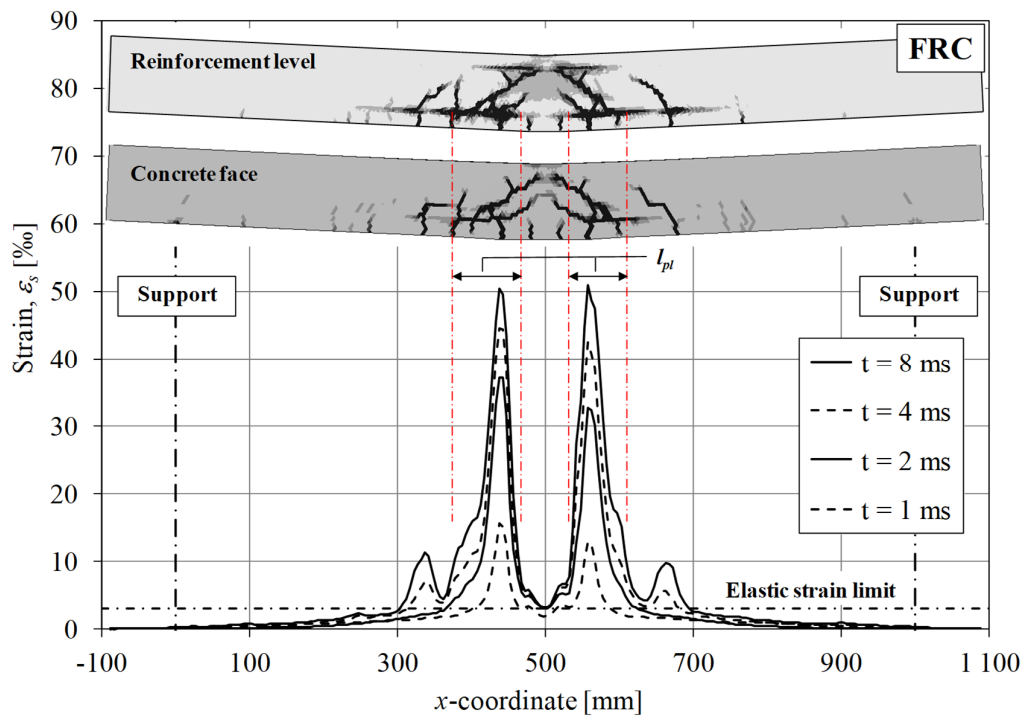
Fig. 14 shows strains in the reinforcement along the length of the RC and FRC beams. Although the total deflection in the RC beam was larger than in the FRC beam, the maximum reinforcement strain in the FRC beam was more than twice as high as in the RC beam. In the RC beam, the maximum reinforcement strain did not exceed 25 ‰, and the strains were rather evenly distributed in the middle of the beam, giving rise to a well-defined plastic hinge with a length l_{pl} of approximately 0.35 m (l_{pl} is here defined as the total distance where $\varepsilon_s \geq 10 \text{ ‰}$). However, for the FRC beam, the maximum reinforcement strain reached 50 ‰, and the length of its plastic hinge was considerably smaller, about 0.20 m.

The difference in response observed is due to different interaction between reinforcement and concrete in the two models. In the RC beam, the strain in the reinforcement damages surrounding concrete; i.e., spalling cracks appear that reduce the interaction stiffness between

540 reinforcement and concrete. This phenomenon enables the reinforcement strain to be more
541 evenly distributed over a longer distance, resulting in a more uniform strain distribution over a
542 larger length. In the FRC beam, the fibres make the concrete much more ductile; its fracture
543 energy is almost 15 times higher than that of the RC beam. Because the fibres prevent spalling
544 cracks from forming, the effective bond between reinforcement and concrete remains more or
545 less intact. A stiffer bond interaction leads to an increased amount of strain localisation, and
546 therefore the maximum reinforcement strain becomes higher. This increase is also evident in
547 Fig. 14 and has previously been observed for statically-loaded beams subjected to bending
548 failure [86,87].



549



550

551 **Fig. 14.** Strain in bottom reinforcement in FE analyses of RC (top) and FRC (bottom)
 552 beams using tetrahedral elements. As comparison, the crack patterns obtained at the
 553 reinforcement level and at the concrete face are shown.

In Section 1, it is concluded that the design of concrete structures subjected to impulse loading needs to make sure that the structure can manage large plastic deformations prior to failure. There are many parameters that affect the plastic deformation capacity of a reinforced concrete structure (e.g., reinforcement ductility (strength ratio f_u/f_y and ultimate strain), bond between reinforcement and concrete, mechanical reinforcement ratio, and structure slenderness); how to predict plastic deformation capacity is its own research field [88–90]. However, one important criterion for obtaining this response is to obtain a large plastic hinge in which the reinforcement can develop plastic strains. Whether the reinforcement or the concrete is critical for the final plastic deformation capacity depends on the reinforcement's mechanical properties and the mechanical reinforcement ratio. Low reinforcement ductility, high concrete strength and low reinforcement amount increase the risk of reinforcement rupture (Fig. 15). Hence, the observation made above is important, since it indicates that the maximum reinforcement strain in reinforced concrete structures may increase due to the presence of fibres – i.e., the risk of reinforcement rupture may increase. Depending on the configuration of the structure, this may have considerable negative effects on the structure's deformation capacity. In this study, the deformation capacities proved to be adequate for both the RC and the FRC beams. However, in a structure with smaller mechanical reinforcement amount, there is increased risk for ruptured reinforcement leading to collapse.

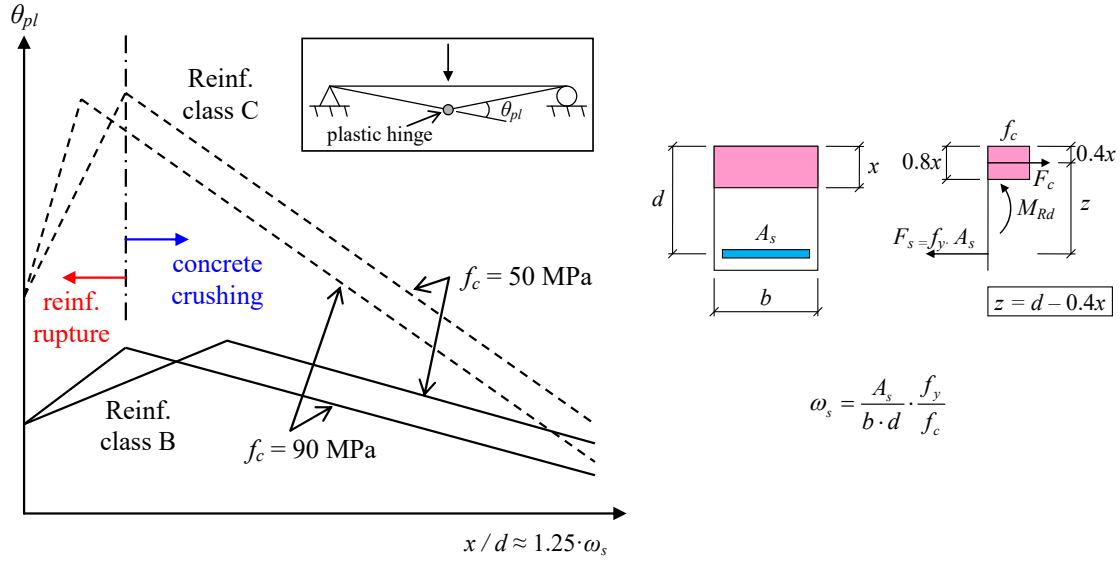


Fig. 15. Schematic illustration of plastic deformation as function of the mechanical reinforcement ratio ω_s for different classes of reinforcement (class C is more ductile than class B) and concrete strength. For each line, the ascending and descending branch indicates reinforcement rupture and concrete crushing, respectively. Based on [71].

In the FE models used here, perfect bond between reinforcement and concrete was assumed. Hence, the bond-slip relation between reinforcement and surrounding concrete was not explicitly incorporated in the model. Nevertheless, the effect of reduced bond is still included in an approximate way since the concrete in the vicinity of the reinforcement bars are affected (cracked) by the force in the reinforcement. In Fig. 14, the effect of reduced bond is indicated by the horizontal cracks at the level of the bottom reinforcement - i.e., spalling cracks. The extension of this zone of reduced bond also agrees well with the location of large reinforcement strains in both the RC and the FRC beam.

5. Conclusions

Based on experiments and numerical analyses of drop weight impact tests of RC and FRC beams, the following conclusions can be drawn.

Digital image correlation (DIC) analysis of high-speed camera images is a very powerful tool for analysing the response of drop weight impact tests. The deformation and crack propagation of the beams tested could be followed in detail.

FE analyses with the material model CDPM2, using tetrahedral elements, effectively captures the response of the impact loaded beams. The use of hexahedral elements is not adequate for representing correct response when diagonal cracks are formed.

The FE analyses showed that the strains in the reinforcement were more evenly distributed and that the length of the plastic hinge was larger in the RC beams than for FRC beams. In the latter, larger maximum strains were also obtained, even though both deflection and crack widths were smaller in the experiments. This finding indicates that there may be an increased risk of reinforcement rupture in FRC structures, a finding that calls for further study.

The CDPM2 material model shows promising results for use in the evaluation of impulse loaded structures; however, there is need for further investigating into how to model the influence of strain rates on concrete properties in general and, in particular on fracture energy.

Acknowledgements

This research has been carried out in collaboration with Chalmers University of Technology and the University of Glasgow. The authors from Chalmers would like to thank the Swedish Civil Contingencies Agency (especially Björn Ekengren and Lars Gråbergs) for financially supporting this study. They would also like to thank a number of people involved in the experiments, namely Jonas Ekström and Sebastian Almfeldt for carrying out the experiments, Mathias Flansbjer for handling the high-speed camera during the experiments and for his help with DIC, Ingemar Löfgren from Thomas Concrete Group for providing the concrete mix design and material casting the beams, and Leo Laine for his valuable advice.

610 **References**

- 611 [1] P.H. Bischoff, S.H. Perry, Compressive behaviour of concrete at high strain rates,
612 Mater. Struct. 24 (1991) 425–450.
- 613 [2] L.J. Malvar, C.A. Ross, Review of strain rate effects for concrete in tension, ACI
614 Mater. J. 95 (1998) 735–739.
- 615 [3] L.J. Malvar, Review of Static and Dynamic Properties of Steel Reinforcing Bars, ACI
616 Mater. J. 95 (1998).
- 617 [4] A. Miyamoto, M. King, M. Fujii, Non-linear dynamic analysis and design concepts for
618 RC beams under impulsive loads, Bull. New Zeal. Soc. Earthq. Eng. 22 (1989) 98–111.
- 619 [5] K. Fujikake, T. Senga, N. Ueda, T. Ohno, M. Katagiri, Study on Impact Response of
620 Reactive Powder Concrete Beam and Its Analytical Model, J. Adv. Concr. Technol. - J
621 ADV CONCR TECHNOL. 4 (2006) 99–108.
- 622 [6] D.M. Cotsovos, N.D. Stathopoulos, C.A. Zeris, Behavior of RC Beams Subjected to
623 High Rates of Concentrated Loading, J. Struct. Eng. 134 (2008) 1839–1851.
- 624 [7] X.X. Zhang, A.M. Abd Elazim, G. Ruiz, R.C. Yu, Fracture behaviour of steel fibre-
625 reinforced concrete at a wide range of loading rates, Int. J. Impact Eng. 71 (2014) 89–
626 96.
- 627 [8] K. Fujikake, B. Li, S. Soeun, Impact Response of Reinforced Concrete Beam and Its
628 Analytical Evaluation, J. Struct. Eng. 135 (2009) 938–950.
- 629 [9] W.-J. Yi, D.-B. Zhao, S.K. Kunnath, Simplified Approach for Assessing Shear
630 Resistance of Reinforced Concrete Beams under Impact Loads., ACI Struct. J. 113
631 (2016) 747.

- 632 [10] P. Isaac, A. Darby, T. Ibell, M. Evernden, Experimental investigation into the force
633 propagation velocity due to hard impacts on reinforced concrete members, *Int. J.*
634 *Impact Eng.* 100 (2017) 131–138.
- 635 [11] G.S.D. Ulzurun, C. Zanuy, M. Johansson, R. Rempling, Impact propagation effects
636 along reinforced concrete beams, in: *IABSE Symp. Guimarães 2019, Towar. a*
637 *Resilient Built Environ. - Risk Asset Manag.* Guimarães, Port., 2019.
- 638 [12] J. Lovén, E.S. Svavarsdóttir, Concrete Beams Subjected to Drop Weight Impact,
639 Comparison of experimental data and numerical modelling, Chalmers University of
640 Technology, Department of Civil and Environmental Engineering, Göteborg, 2016.
- 641 [13] P. Grassl, M. Johansson, J. Leppänen, On the numerical modelling of bond for the
642 failure analysis of reinforced concrete, *Eng. Fract. Mech.* 189 (2018) 13–26.
- 643 [14] J.M. Biggs, *Introduction to Structural Dynamics*. McGraw-Hill, New-York, USA,
644 1964.
- 645 [15] D. Cormie, G. Mays, P. Smith, *Blast Effects on Buildings*, Second Edition. Thomas
646 Telford Ltd, London, UK, 2009.
- 647 [16] DOD, *Structures to Resist the Effects of Accidental Explosions*. UFC 3-340-02,
648 Department of Defence, USA, 2008.
- 649 [17] FKR, Swedish Fortifications Agency. *Building Regulations FKR 2011*. Dnr.
650 4535/2011 (In Swedish). Eskilstuna, Sweden, 2011.
- 651 [18] N. Kishi, H. Mikami, K.G. Matsuoka, T. Ando, Impact behavior of shear-failure-type
652 RC beams without shear rebar, *Int. J. Impact Eng.* 27 (2002) 955–968.
- 653 [19] S. Saatci, F.J. Vecchio, Effects of Shear Mechanisms on Impact Behavior of
654 Reinforced Concrete Beams., *ACI Struct. J.* 106(1) (2009) 78–86.

- 655 [20] J. Magnusson, M. Hallgren, A. Ansell, Shear in concrete structures subjected to
656 dynamic loads, *Struct. Concr.* 15 (2014) 55–65.
- 657 [21] K. Shivakumar, W. Elber, W. Illg, Prediction of Impact Force and Duration During
658 Low Velocity Impact On Circular Composite Laminates, *J. Appl. Mech. Trans. ASME.*
659 52 (1985).
- 660 [22] J. Mier, A. Pruijssers, H. Reinhardt, T. Monnier, Load-Time Response of Colliding
661 Concrete Bodies, *J. Struct. Eng.* 117 (1991) 354–374.
- 662 [23] T.M. Pham, H. Hao, Influence of global stiffness and equivalent model on prediction of
663 impact response of RC beams, *Int. J. Impact Eng.* 113 (2018) 88–97.
- 664 [24] H. Li, W. Chen, H. Hao, Dynamic response of precast concrete beam with wet
665 connection subjected to impact loads, *Eng. Struct.* 191 (2019) 247–263.
- 666 [25] W. Zhao, J. Qian, P. Jia, Peak Response Prediction for RC Beams under Impact
667 Loading, *Shock Vib.* 2019 (2019) 1–12.
- 668 [26] M. Johansson, L. Laine, Bebyggelsens motståndsförmåga mot extrem dynamisk
669 belastning Del 3: Kapacitet hos byggnader, (The resistance of housing settlement
670 subjected to extreme dynamic loading. Part 3: Building capacity. In Swedish), 2012.
- 671 [27] L. Ågårdh, K.G. Bolling, L. Laine, Fibre reinforced concrete beams loaded by impact,
672 Experiments and FE-modelling, Defence research establishment, FOA-R--9700587-
673 311--SE, Tumba, Sweden, 1997.
- 674 [28] S. Tachibana, H. Masuya, S. Nakamura, Performance based design of reinforced
675 concrete beams under impact, *Nat. Hazards Earth Syst. Sci.* 10 (2010) 1069–1078.
- 676 [29] S.M.M. Soleimani, N. Banthia, A Novel Drop Weight Impact Setup for Testing
677 Reinforced Concrete Beams, *Exp. Tech.* 38 (2014) 72–79.

- 678 [30] S. Das Adhikary, B. Li, K. Fujikake, Dynamic behavior of reinforced concrete beams
679 under varying rates of concentrated loading, *Int. J. Impact Eng.* 47 (2012) 24–38.
- 680 [31] G.S.D. Ulzurrin, C. Zanuy, Enhancement of impact performance of reinforced
681 concrete beams without stirrups by adding steel fibers, *Constr. Build. Mater.* 145
682 (2017) 166–182.
- 683 [32] B. Barr, A. Bouamrata, Development of a repeated dropweight impact testing
684 apparatus for studying fibre reinforced concrete materials, *Composites.* 19 (1988) 453–
685 466.
- 686 [33] X.X. Zhang, G. Ruiz, R.C. Yu, A New Drop-Weight Impact Machine for Studying
687 Fracture Processes in Structural Concrete, *Strain.* 46 (2008) 252–257.
- 688 [34] X.X. Zhang, A.M. Abd Elazim, G. Ruiz, R.C. Yu, Fracture behaviour of steel fibre-
689 reinforced concrete at a wide range of loading rates, *Int. J. Impact Eng.* 71 (2014) 89–
690 96.
- 691 [35] P.L. Reu, T.J. Miller, The application of high-speed digital image correlation, *J. Strain*
692 *Anal. Eng. Des.* 43 (2008) 673–688.
- 693 [36] J. Ekström, Blast and Impact Loaded Concrete Structures - Numerical and
694 Experimental Methodologies for Reinforced Plain and Fibre Concrete Structures,
695 Chalmers University of Technology, 2017.
- 696 [37] L.J. Malvar, J.E. Crawford, J.W. Wesevich, D. Simons, A plasticity concrete material
697 model for DYNA3D, *Int. J. Impact Eng.* 19 (1997) 847–873.
- 698 [38] L.E. Schwer, Y.D. Murray, A three-invariant smooth cap model with mixed hardening,
699 *Int. J. Numer. Anal. Methods Geomech.* 18 (1994) 657–688.
- 700 [39] L.F. Pereira, J. Weerheijm, L.J. Sluys, A numerical study on crack branching in quasi-

701 brittle materials with a new effective rate-dependent nonlocal damage model, Eng.
702 Fract. Mech. 182 (2017) 689–707.

703 [40] L.F. Pereira, J. Weerheijm, L.J. Sluys, Simulation of compaction and crushing of
704 concrete in ballistic impact with a new damage model, Int. J. Impact Eng. 111 (2018)
705 208–221.

706 [41] N. Gebbeken, M. Ruppert, A new material model for concrete in high-dynamic
707 hydrocode simulations, Arch. Appl. Mech. (Ingenieur Arch. 70 (2000) 463–478.

708 [42] P. Grassl, M. Jirásek, Damage-plastic model for concrete failure, Int. J. Solids Struct.
709 43 (2006) 7166–7196.

710 [43] J. Lee, G.L. Fenves, Plastic-Damage Model for Cyclic Loading of Concrete Structures,
711 J. Eng. Mech. 124 (1998) 892–900.

712 [44] J. Lubliner, J. Oliver, S. Oller, E. Oñate, A plastic-damage model for concrete, Int. J.
713 Solids Struct. 25 (1989) 299–326.

714 [45] H. Othman, H. Marzouk, Applicability of damage plasticity constitutive model for
715 ultra-high performance fibre-reinforced concrete under impact loads, Int. J. Impact
716 Eng. 114 (2018) 20–31.

717 [46] J. Ožbolt, A. Sharma, H.-W. Reinhardt, Dynamic fracture of concrete – compact
718 tension specimen, Int. J. Solids Struct. 48 (2011) 1534–1543.

719 [47] J. Ožbolt, A. Sharma, Numerical simulation of reinforced concrete beams with
720 different shear reinforcements under dynamic impact loads, Int. J. Impact Eng. 38
721 (2011) 940–950.

722 [48] J. Feng, W. Yao, W. Li, W. Li, Lattice discrete particle modeling of plain concrete
723 perforation responses, Int. J. Impact Eng. 109 (2017) 39–51.

- 724 [49] K. Kim, J.E. Bolander, Y.M. Lim, Failure simulation of RC structures under highly
725 dynamic conditions using random lattice models, *Comput. Struct.* 125 (2013) 127–136.
- 726 [50] K.-J. Bathe, *Finite Element Procedures*. Prentice Hall, Englewood Cliffs, New Jersey,
727 USA, 1996.
- 728 [51] P. Grassl, D. Xenos, U. Nyström, R. Rempling, K. Gylltoft, CDPM2: A damage-
729 plasticity approach to modelling the failure of concrete, *Int. J. Solids Struct.* 50 (2013)
730 3805–3816.
- 731 [52] P. Grassl, U. Nyström, R. Rempling, K. Gylltoft, A damage-plasticity model for the
732 dynamic failure of concrete, in: *Proc. 8th Int. Conf. Struct. Dyn. EURODYN 2011*,
733 2011: pp. 4–6.
- 734 [53] B. İrhan, J. Ožbolt, D. Ruta, 3D finite element simulations of high velocity projectile
735 impact, *Int. J. Solids Struct.* 72 (2015) 38–49.
- 736 [54] W. Luo, V.T. Chau, Z.P. Bažant, Effect of high-rate dynamic comminution on
737 penetration of projectiles of various velocities and impact angles into concrete, *Int. J.*
738 *Fract.* 216 (2019) 211–221.
- 739 [55] R. Shao, C. Wu, Y. Su, Z. Liu, J. Liu, S. Xu, Numerical analysis on impact response of
740 ultra-high strength concrete protected with composite materials against steel ogive-
741 nosed projectile penetration, *Compos. Struct.* 220 (2019) 861–874.
- 742 [56] A. Nishida, Z. Kang, M. Nagai, H. Tsubota, Y. Li, Evaluation of local damage to
743 reinforced concrete panels subjected to oblique impact by soft missile, *Nucl. Eng. Des.*
744 350 (2019) 116–127.
- 745 [57] R. Hosseinzadeh, M.M. Shokrieh, L. Lessard, Damage behavior of fiber reinforced
746 composite plates subjected to drop weight impacts, 66 (2006) 61–68.

- 747 [58] L. Schwer, Prediction of Air Blast Loaded Concrete Slab Response Using Six LS-
748 DYNA Concrete Models. Tech. rep., pp. 1-32, 2013.
- 749 [59] M. Jirásek, P. Grassl, Evaluation of directional mesh bias in concrete fracture
750 simulations using continuum damage models, *Eng. Fract. Mech.* 75 (2008) 1921–1943.
- 751 [60] J.G. Rots, Computational modeling of concrete fracture, Delft University of
752 Technology, 1988.
- 753 [61] P. Grassl, Quasi-static three point bending LS-Dyna analyses with MAT CDPM (MAT
754 273) using tetra- and hexahedral meshes., Research report, School of Engineering,
755 University of Glasgow, 2016.
- 756 [62] Q. Fang, J. Zhang, Three-dimensional modelling of steel fiber reinforced concrete
757 material under intense dynamic loading, *Constr. Build. Mater.* 44 (2013) 118–132.
- 758 [63] J. Ožbolt, J. Bošnjak, E. Sola, Dynamic fracture of concrete compact tension specimen:
759 Experimental and numerical study, *Int. J. Solids Struct.* 50 (2013) 4270–4278.
- 760 [64] G. Ruiz, A. Pandolfi, M. Ortiz, Three-dimensional cohesive modeling of dynamic
761 mixed-mode fracture, *Int. J. Numer. Methods Eng.* 52 (2001) 97–120.
- 762 [65] F.J. Lozano, J.A. Makdesi, Concrete Beams Subjected to Drop-Weight Impact and
763 Static Load: Structural Behavior and Plastic Rotational Capacity from Experiments and
764 Finite Element Analysis, Chalmers University of Technology, 2017.
- 765 [66] Software ARAMIS., (n.d.). <http://www.gom.com/3d-software/gom-correlate.html>
766 (accessed June 25, 2018).
- 767 [67] CEN 2004, EN 12390-3: Testing hardened concrete - Part 3: Compressive strength of
768 test specimens, 2009.

- 769 [68] CEN 2004, EN 12390-6: Testing hardened concrete - Part 6: Tensile splitting strength
770 of test specimens, 2009.
- 771 [69] I. Löfgren, J.F. Olesen, M. Flansbjer, Application of WST-method for fracture testing
772 of fibre- reinforced concrete, Chalmers University of Technology, Department of
773 Structural Engineering and Mechanics, Report 04:13, 2004.
- 774 [70] RILEM TC 162-TDF. Brite Euram Project nr: BE 97-4163, Test and Design Methods
775 for Steel Fibre Reinforced Concrete, ISBN 90-5682-358-2, June, 2002.
- 776 [71] CEN, EN 1992-1-1, Design of concrete structures - Part 1-1: General rules and rules
777 for buildings, (2004).
- 778 [72] M. Jirásek, Z.P. Bažant, Inelastic analysis of structures., John Wiley and Sons,
779 Chichester, 2002.
- 780 [73] P. Menétrey, K.J. Willam, A triaxial failure criterion for concrete and its
781 generalization, ACI Struct. J. 92 (1995) 311–318.
- 782 [74] P. Ladeveze, A damage computational approach for composites: Basic aspects and
783 micromechanical relations, Comput. Mech. 17 (1995) 142–150.
- 784 [75] U. Häussler-Combe, T. Kühn, Modeling of strain rate effects for concrete with
785 viscoelasticity and retarded damage, Int. J. Impact Eng. 50 (2012) 17–28.
- 786 [76] T. Li Piani, J. Weerheijm, L.J. Sluys, Dynamic simulations of traditional masonry
787 materials at different loading rates using an enriched damage delay: theory and
788 practical applications, Eng. Fract. Mech. 218 (2019) 21.
- 789 [77] G. Cusatis, Strain-rate effects on concrete behavior, Int. J. Impact Eng. 38 (2011) 162–
790 170.

- 791 [78] CEB, CEB-FIB Model Code 1990. Design Code, Thomas Telford, Lausanne,
792 Switzerland, 437 pp, 1993.
- 793 [79] Z.P. Bažant, B. Oh, Crack band theory for fracture of concrete, Mater. Struct. 16
794 (1983).
- 795 [80] S.T. Pietruszczak, Z. Mróz, Finite element analysis of deformation of strain-softening
796 materials, 1981.
- 797 [81] K. Willam, N. Bićanić, S. Sture, Composite fracture model for strain-softening and
798 localised failure of concrete, in: E. Hinton, D.R.J. Owen (Eds.), Comput. Model. Reinf.
799 Concr. Struct., Pineridge Press, Swansea, 1986: pp. 122–153.
- 800 [82] M. Jirásek, M. Bauer, Numerical aspects of the crack band approach, Comput. Struct.
801 110–111 (2012) 60–78.
- 802 [83] G.R. Johnson, W.H. Cook, Fracture characteristics of three metals subjected to various
803 strains, strain rates, temperatures and pressures, Eng. Fract. Mech. 21 (1985) 31–48.
- 804 [84] CEB, Concrete Structures under Impact and Impulsive Loading. CEB Bulletin
805 d'Information No 187, Lausanne, Switzerland, 1988.
- 806 [85] LS-DYNA., (n.d.). <http://www.lstc.com/> (accessed June 25, 2018).
- 807 [86] A. Meda, F. Minelli, G.A. Plizzari, Flexural behaviour of RC beams in fibre reinforced
808 concrete, Compos. Part B Eng. 43 (2012) 2930–2937.
- 809 [87] C.G. Berrocal, I. Löfgren, K. Lundgren, The effect of fibres on steel bar corrosion and
810 flexural behaviour of corroded RC beams, Eng. Struct. 163 (2018) 409–425.
- 811 [88] CEB, Ductility of Reinforced Concrete Structures. CEB Bulletin d'information No
812 242, Lausanne, Switzerland, 1998.

- 813 [89] Bigaj A.J., Structural Dependence of Rotational Capacity of Plastic Hinges in RC
814 Beams and Slabs, TU Delft, Civil Engineering and Geosciences, Delft, The
815 Netherlands, 1999.
- 816 [90] Plem E., The Rotational Capacity of Plastic Hinges in Reinforced Concrete Beams: A
817 Theoretical Study. Lund Institute of Technology, Department of Structural Mechanics,
818 Vol. R81-1, Lund, Sweden, 1981.

819 **Appendix**

820 **Table A.1**

821 Data summary for the self-compacting concrete mixtures.

	Plain	Fibre reinforced
Constituents	Amount [kg/m ³]	Amount [kg/m ³]
Cement	335	335
Limestone filler	160	160
Sand	747.3	741.1
Aggregates		
4 – 8 mm	268.9	266.8
8 – 16 mm	717.1	711.4
Superplasticiser	5.36	5.36
Fibre	-	40
Water	184.3	184.3
w-c ratio	0.55	0.55

822

823 **Table A.2**

824 Geometry for the drop weight.

Length	260 [mm]
Diameter	80 [mm]
Weight	10.1 [kg]
Radius of the head	400 [mm]

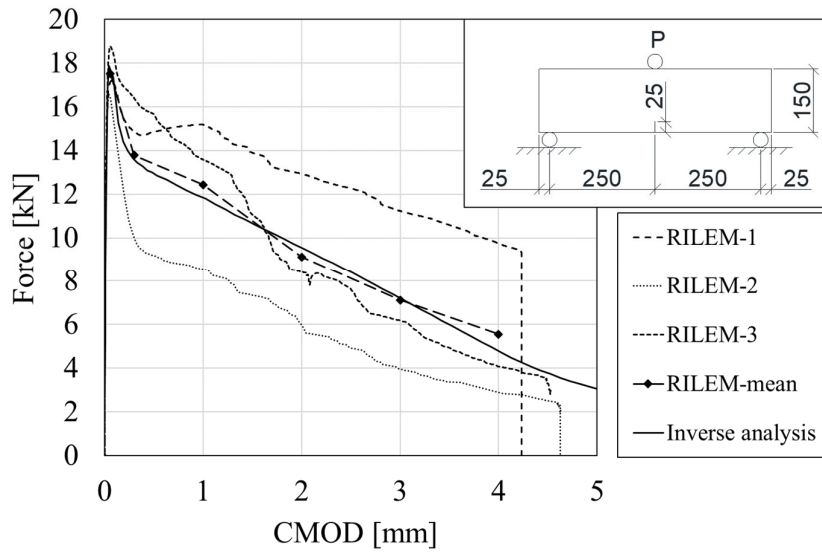


Fig. A.1. Force – CMOD curve from RILEM beams, and results from adaptive inverse analysis.

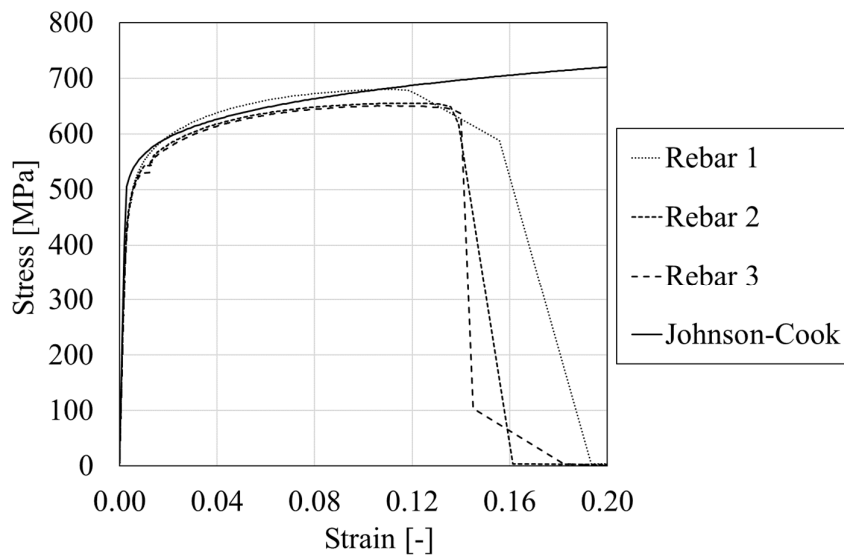


Fig. A.2. Stress-strain curve for the reinforcement: measured values (3 bars) vs. input data to FE analyses for the material model Johnson-Cook.